Radiat Environ Biophys (2016) 55:229–241
DOI 10.1007/s00411-016-0637-6

ORIGINAL ARTICLE

Risk to fragmented DNA in dry, wet, and frozen states from computed tomography: a comparative theoretical study

Johann Wanek[1] · **Frank Jakobus Rühli**[1]

Received: 8 September 2015 / Accepted: 30 January 2016 / Published online: 16 February 2016

Abstract Computed tomography represents the gold standard in forensic and palaeopathological diagnosis. However, the X-rays used may affect the DNA quality through fragmentation and loss of genetic information. Previous work showed that the effects of ionizing radiation on dry DNA are non-significant with $P < 10^{-8}$, which cannot be detected by means of polymerase chain reaction methods. In the present paper, complete analytical model that characterizes radiation effects on fragmented DNA in dry, wet, and frozen states is described. Simulation of radiation tracks in water phantom cells was performed using the Geant4-DNA toolkit. Cell hits by electrons with energies between 5 and 20 keV were simulated, and the formation of radiolytic products was assessed at a temperature of 298 K. The diffusion coefficient and the mean square displacement of reactive species were calculated by Stokes–Einstein–Smoluchowski relations at 273 K. Finally, DNA fragment damage was estimated using the density distribution of fragments calculated from atomic force microscopy images. The lowest probability of radiation-induced DNA damage was observed for dry state, with a range from 2.5×10^{-9} to 7.8×10^{-12} at 298 K, followed by that for frozen state, with a range from 0.9 to 4×10^{-7} at 273 K. The highest probability of radiation-induced DNA damage was demonstrated for fragmented DNA in wet state with a range from 2 to 9×10^{-7} at 298 K. These results significantly improve the interpretation of CT imaging in future studies in forensic and palaeopathological science.

✉ Johann Wanek
johann.wanek@iem.uzh.ch

[1] Institute of Evolutionary Medicine, University of Zurich, Winterthurerstrasse 190, 8057 Zurich, Switzerland

Keywords Radiation risk · Computed tomography · Fragmented DNA · Ancient remains · Geant4-DNA

Introduction

X-ray imaging has a long tradition in palaeoradiology and was first performed by the physicist Wilhelm Koenig of Frankfurt in 1896 to examine a mummified child and a cat (Koenig 1896). In the past, progress in palaeoradiology was influenced by the development of sophisticated clinical imaging systems such as computed tomography (CT) and micro-CT (mCT) with X-ray spectra corresponding to 80–140 kVp (CT) and 40–70 kVp (mCT), respectively. At present, 3D techniques are widely employed and it is believed that these increase the diagnostic yield and confidence in the palaeopathological assessment of human skeletal remains. Both micro-CT and CT use X-rays for imaging and are considered as non-destructive methods from the macroscopic viewpoint. Not surprisingly, such techniques have become the gold standard in diagnostics of irreplaceable ancient mummies. However, it should be recalled that X-rays include energies much higher than the ionization potential of DNA ($\approx$8 eV) (Miller et al. 1994); X-rays are considered to be "ionizing" and may damage DNA molecules by direct and indirect actions of radiation. Therefore, CT scans can be considered as a destructive method at micro- and nanoscale, especially when indirect effects of radiation become dominant in CT studies of wet and frozen objects (Alpen 1998, p. 120). Consequently, researchers have successfully used non-ionizing imaging techniques such as magnetic resonance or terahertz imaging (Rühli et al. 2007; Oehrstroem et al. 2010), a scientific breakthrough given that the ancient remains are mostly desiccated. To date, CT imaging is hard to be replaced, due

to the insufficient discrimination of hard and soft tissue obtained by non-ionizing techniques.

In general, CT-induced DNA lesions of ancient remains depend on their physical state of their surrounding (e.g. dry, wet, or frozen tissue) and on the quality of the DNA preservation (Wanek et al. 2013). There are different types of mummification techniques to slow down the decomposition of soft tissue and to preserve the DNA. In this work, the statistical method used does not distinguish between anthropogenic or natural mummification and the different kinds of body desiccation. This work is focused on the understanding of physicochemical phenomena of radiation in the different physical states of preservation. Important parameters which affect radiation-induced DNA damage are the tissue density (Wanek et al. 2013), and the physical state of ancient remains absorbing ionizing radiation. Relevant physical parameters such as temperature (in Kelvin) and relative humidity (RH) are defined as the following: dry tissue (298 K, 60 % RH); frozen tissue (273 K, $\approx$100 % RH); and wet tissue (298 K, $\approx$100 % RH).

The radiation damage to dry objects was successfully investigated in our previous work (Wanek et al. 2013), as depicted in the right column in Fig. 1. In the present study, the radiation damage to wet and frozen objects is assumed to be higher than the aDNA damage in dry objects due to the "indirect action" of ionizing radiation that plays a more dominant role than the "direct action" (Kudryashov 2008). However, the radiation damage to frozen objects in Fig. 1 is assumed to be smaller in comparison with wet objects according to the Arrhenius law in Eq. (5). Figure 1 summarizes the hypothetical radiation damage to objects in different physical states.

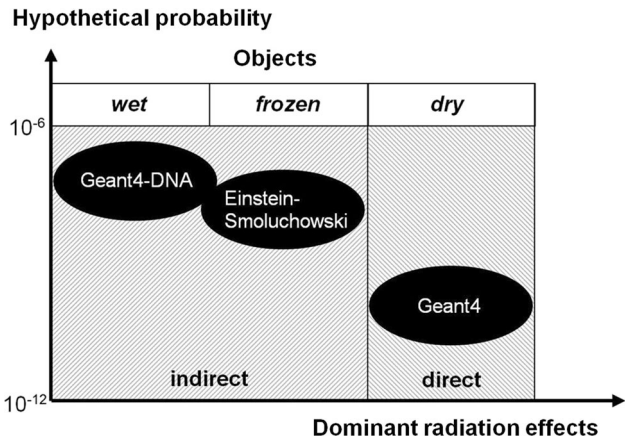

Fig. 1 Diagram shows the hypothetical probability for radiation-induced damage of fragmented DNA under different physical states following CT exposure. Each *ellipsis* indicates the estimated probability level and the methods used. The damage to dry objects is investigated in our previous study (Wanek et al. 2013). Geant4 (2015) and Geant4-DNA are computational stochastic methods. Einstein–Smoluchowski laws are used to calculate the damage to frozen objects

There are two research questions that had to be answered by the present study:

1. Which factors affect the radiation-induced aDNA damage in liquid cells at room temperature?
2. Which factors affect the radiation-induced aDNA damage in frozen cells at freezing temperature?

The hypotheses involved are:

(1) The temperature of objects affects the molecular diffusion of radiation-induced reactive species.

(2) Indirect radiation effects increase the probability of aDNA damage.

In this study, the effects of CT imaging on mummified remains were investigated theoretically under three general conditions of irradiation: in dry, wet, and frozen states.

Materials and methods

General considerations

Radiation damage classification plays an important role in the cost–benefit analysis not only for CT imaging studies in forensic and palaeophatological science but also in everyday clinical radiology. By knowing the CT-induced damage to objects in liquid, frozen, or dry state, researchers may determine a system of hierarchies before performing CT examinations and genetic analyses. Radiation-related damage to aDNA in different physical states has never been addressed before and may be valuable for choosing the optimal genetic analysis method.

Mummified remains in dry state

From a physical point of view, desiccated mummified remains are characterized by small density differences between hard and soft tissue. As an example, the density difference between bone and muscle tissue in desiccated remains ($1.8 - 1.3 = 0.5$ g/cm^3) is similar to that in normal tissue ($1.8 - 1.0 = 0.8$ g/cm^3) (Wanek et al. 2013). Dehydrated cells with a large number of DNA fragments [e.g. 40×10^6 fragments at a length of 150 base pairs (bp)] are typically embedded in brittle tissue. The average fragment size of mummified DNA is often in the range between 100 and 200 bp (Pääbo 1989; Haack et al. 2000). Clearly, such low quality of DNA with a large number of fragments affects the reliability of the polymerase chain reaction (PCR) method in forensic and palaeopathological studies. Researchers have noted that "only mummification

by desiccation provides high quality DNA" (Shved et al. 2014) as demonstrated by salt mummification. Further degradation of the historically valuable DNA can be stopped by specific environmental conditions; for example, the British Museum recommends a relative humidity of 50 % and a temperature range between 18 and 25 °C for dry remains, for Egyptian mummies (Rae 1996).

(a) The effect of CT scans on dry DNA

In the past, the impact of low-dose ionizing radiation on dry specimens was investigated by several research groups (Grieshaber et al. 2008; Paredes et al. 2012; Ziegler et al. 2013) using molecular analysis techniques. However, the extremely small effects of CT imaging on ancient DNA (aDNA) are not readily quantifiable with the current PCR method. To overcome this limitation, the radioinduced aDNA damage, which mainly originates from secondary electron hits was estimated using stochastic Monte Carlo (MC) simulations and theories, for example probability rules and target theory (Lea 1955). Our previous work entitled "Direct Action of Radiation on Mummified Cells: Modelling of Computed Tomography by Monte Carlo Algorithms" (Wanek et al. 2013) was focused on desiccated human remains. The main findings described there indicate the dominance of single cell hits with $P(1)_{\text{dry\_cell}} = 0.28$ after CT simulation assuming Poisson distribution (Wanek et al. 2013). The probability for a single DNA hit was estimated by $P(1)_{\text{DNA}} = v_{\text{DNA}}/V_{\text{cell}}$, where v_{DNA} is the DNA volume and V_{cell} is the cell volume (EPFL 2012). Thus, the probability of a non-fragmented DNA damage (NFD) was approximated with $P(\text{NFD}) \approx P(1)_{\text{dry\_cell}} \times P(1)_{\text{DNA}} \approx 0.28 \times 0.012 \approx 0.0034$. Note that these results were approximately in line with those from the X-ray risk calculator for abdomen CT of a 20-year-old female with $P(\text{NFD}) \approx 0.0014$ (Hanley 2013). These examples are related to direct effects of low-dose ionizing radiation and NFD. In the case of fragmented DNA (e.g. aDNA), the probability to hit the many nano-volumes present in the cell is dramatically reduced; a more precise explanation is given in the next section.

(b) Direct action of ionizing radiation on fragmented DNA

Direct action of ionizing radiation is characterized by damage to molecules through direct absorption of energy by the molecules (Kudryashov 2008). Ionizing radiation may transfer kinetic energy to atoms or molecules in the so-called physical stage ($<10^{-13}$ s) (Kudryashov 2008). In the physical stage, secondary electrons may ionize or excite atoms and DNA molecules. The probability of degradation of aDNA by direct radiation action on dry remains was evaluated using MC simulations (Wanek et al. 2013) with anthropomorphic cell phantoms. It was shown that the average probability of damaging fragmented DNA (FD) can be expressed as

$$P(\text{FD}) = [P(\text{NFD}) \times 1/n] \propto v_{\text{DNA\_FR}} \quad (1)$$

$P(\text{FD})$ is proportional to the volume of the DNA fragment $v_{\text{DNA\_FR}}$, which is calculated by dividing the volume of normal DNA (EPFL 2012) by the number of fragments n ($v_{\text{DNA\_FR}} = 6.41 \times 10^{-18}$ m^3/n).

As shown in Eq. (1), the average probability of destroying the fragmented DNA is about 1/n times lower than the probability of damaging normal non-fragmented DNA in living cells, abbreviated here by $P(\text{NFD})$. Equation (1) is used to summarize the radiation-induced direct effects on dry DNA as a function of the number of fragments. According to the probability rule, the overall probability of damaging all fragments (DAF) within a cell tends towards zero in Eq. (2) with increases in the number of cell hits m, as demonstrated by the Poisson distribution in Wanek et al. (2013).

$$\begin{aligned} P(\text{DAF}) &= P(\text{NFD}) \times P(\omega_1) \times P(\omega_2) \times \cdots \times P(\omega_n) \\ &= P(\text{NFD}) \times [P(\omega_n)]^m \rightarrow 0 \end{aligned} \quad (2)$$

where $m = \{0, 1, 2, \ldots\}$ is the number of cell hits and ω is the DNA fragment. As also shown in our previous work, the radiation sensitivity of dry objects depends mainly on the DNA fragment size and the number of cell hits, but less on the density of the tissue surrounding the cell nucleus or on X-ray tube voltage.

In general, the determination of the radiation sensitivity of ancient cells and aDNA at low doses presupposes the consideration of worst-case scenarios, in order to quantify the small radiation effects. Millions of DNA fragments in the cell make the ancient DNA insensitive against low-dose radiation because only a few fragments may be damaged during X-ray imaging by direct action of radiation (Wanek et al. 2013). To simulate worst-case scenarios, it is assumed that each DNA fragment hit leads to a double strand break. This approach is in conformance with the target theory defined by Lea (1955).

Mummified remains in wet and frozen states: role of indirect effects of ionizing radiation

In contrast to direct effects of ionizing radiation, indirect effects play the dominant role in wet and frozen states of ancient remains. Wet mummies can be found as bog bodies in northern Europe and range in date "widely from 900 BC to 1800 AD" (Brothwell 1996, p. 161); such mummies are characterized by different conservation methods. Several natural mummified bodies under wet conditions were also found in China (Than 2011). One of the most prominent frozen mummies, recovered from a glacier in the Italian Alps, is a Neolithic Iceman called Oetzi (3200 BC)

(Spindler 2000). Under wet and frozen conditions, hydrolytic and oxidative damage increases (Willerslev et al. 2004), and such chemical modifications influence the indirect action of ionizing radiation which leads, after the ionisation and excitation of water molecules, to the formation of large quantities of highly reactive chemical products (Eqs. 3, 4) such as the hydrogen radical H· and the hydroxyl radical OH· (Hutchinson 1960). Such free radicals contain one unpaired electron, often depicted with an odd number of electrons around the oxygen atom. Exposure of wet or frozen objects to CT radiation leads to the production of numerous oxygen-based radical species, with the hydroxyl radicals being most important (Foote et al. 1995). As demonstrated by an empirical model (Yamaguchi et al. 2005), there is a strong increase in the number of OH· radicals produced by water radiolysis (quantified by the so-called *G*-value given in molecules per 100 eV) where the energy of incident electrons ranges from 5 to 20 keV (Yamaguchi et al. 2005). This outcome is supported by our previous work, which showed that the range of absorbed energy in wet cells is similar (Wanek et al. 2013). Electrons with energies less than 7.4 eV may recombine until thermalization and formation of hydrated electrons (Nikjoo et al. 1996).

(a) The physico-chemical stage

Fast events such as recombination processes of radicals as well as atomic and electronic rearrangements occur in the so-called physico-chemical stage (1 fs to 1 ps) (Karamitros et al. 2011). Typical dissociation reactions in water are shown in Eqs. (3) and (4). Foote et al. (1995) found that the major reaction pathway mainly involves the "abstraction of an H-atom from a C–H bond" in the deoxyribose phosphate moiety of the DNA molecule. The formation of reactive free radicals in water due to X-ray exposure is:

$$H_2O \rightarrow H_2O^+ + e^- \quad (3)$$

The positive ion H_2O^+ in Eq. (3) may dissociate to two mobile radicals: the hydrogen H· and the hydroxyl radical OH·.

$$H_2O^+ \rightarrow H\cdot + OH\cdot \quad (4)$$

Note that the reactivity of the hydroxyl radical has "not been widely studied in frozen aqueous solution" (Kahan et al. 2010, p. 843).

(b) The chemical stage

Reactive substances may diffuse or interact with DNA molecules by breaking chemical bonds in the timescale from 1 ps to 100 ns (Mozumder and Hatano 2004). This stage is called "chemical stage", and all reactions in this time range were simulated for a step of 1.5 ns as demonstrated also by Incerti (2014). According to Karamitros et al. (2011), the changes of radiochemical yields (e.g. *G*-value of OH·) between the time points of 100 ns and 1 µs are negligible. Draganic et al. (1993, p. 87) have underlined the different radiolytic behaviours of liquid water and ice, which "influence the fate of the primary species formed". These authors stress that hydroxyl radicals or hydrogen atoms in ice are also "mobile and cause oxidations or other chemical changes" (Draganic et al. 1993, p. 88), similarly to the situation in liquid water. This is in conformance with Willerslev's review reporting that permafrost ice contains 3–8 % unfrozen water (Willerslev et al. 2004) and this fact may lead to "spontaneous hydrolytic damage" (Willerslev et al. 2004, p. 141) of the DNA such as through backbone cleavage. The difference from liquid water is the rigid structure of ice, which leads to radiation-induced yields reduced by a factor of 10 in ice and frozen aqueous solutions (Draganic et al. 1993). The relationship between reaction rate and temperature will be discussed more in detail using the Arrhenius formula in Eq. (5).

(c) Energy deposition in water

In the case of low-LET (linear energy transfer) radiation such as X-rays, the ionization of water molecules is predominantly ($\approx$70 %) responsible for DNA damage in living objects (Gunderson and Tepper 2012). In order to simulate indirect actions of ionizing radiation on ancient remains, electron tracks with different incident energies must be generated in water cell phantoms. Energy deposition in water by electrons occurs as spurs, blobs, and short tracks depending on the amount of energy deposited in the biological system (Mozumder and Magee 1966). For example, track entities formed by electrons with energies in the range from 6 to 100 eV are called spurs which expand with time due to diffusion of chemical species (Samuel and Magee 1953). Absorption of higher energies by secondary electrons in water is called blobs (100–500 eV) and short tracks (500–5000 eV) (Samuel and Magee 1953).

(d) Diffusion of chemical species

The diffusion of chemical species (chemical stage) must be simulated at 298 K using Monte Carlo technique. A single electron track inside a phantom cell interacts with water molecules by deposition of energy as described by Mozumder and Magee (1966). It is expected that chemical species are arranged around the electron track. In the simulation, the resulting time-dependent inhomogeneous spatial and chemical structure is surrounded by an envelope representing the cross-sectional area. Using the top and side cross-sectional area, a cylinder containing the volume of risk (VOR) can be approximated. To determine the changes of the produced chemical species at different temperatures (273 and 298 K), the ratio of VOR_{273}/VOR_{298} can be calculated using Stokes–Einstein and

Smoluchowski law. Note that the MC simulation done in the present work was only validated for ambient temperature (298 K).

(e) Radical reaction with DNA fragments

Ancient DNA is composed of millions of fragments which are located within and outside the nucleus. In practice, the DNA has decomposed with time depending on the environmental condition and the mummification technique used. In contrast to the work of Michalik et al. (1995), Semsarha et al. (2014) and Bernal et al. (2015), where DNA models represented different conformational states, such a high number of aDNA fragments could not be modelled analytically in the present study. In contrast, the DNA fragment concentration (fragments/μm^3) in liquids was determined using images from atomic force microscopy (AFM) measurements. The number of affected DNA fragments is the product of the volume of risks (VORs) and the DNA fragment concentration. It is assumed that DNA fragments are homogeneously distributed in the cell.

Again, this approach assumes a worst-case scenario, which means that all OH· radicals are able to react with DNA fragments independent of the reaction radius calculated by Michalik et al. (1995). It presupposes that the VOR is a subset of the volume formed by DNA fragments.

(f) Reaction rate as a function of temperature

According to the Arrhenius equation [Eq. (5)], the reaction rate (k) of chemical reactions depends on the temperature T (K) and the activation energy E_a (Brown and LeMay 1997).

$$k = A \exp(-E_a/\mathrm{RT}) \quad (5)$$

where A is the frequency factor (i.e. the probability of a molecular collision leading to a reaction) and R is the universal gas constant ($R = 8.314$ J/mol K). It is interesting to estimate the reaction rate of chemical reactions in frozen bodies to understand the relevance of the indirect action of ionizing radiation at low temperatures. As an example, the iceman Oetzi is preserved at −6 °C and 98 % humidity (Samadelli et al. 2015); his body is rigidly frozen. The temperature of wet objects during CT exposure may have a significant impact on the chemical yields produced. Based on Eq. (5), the chemical activities for the temperatures $T_1 = 277$ K (4 °C) and $T_2 = 267$ K (−6 °C) can be calculated, to demonstrate the decrease in reaction rates, k_1 and k_2, of radicals in a frozen body (e.g. Oetzi) as a function of T_2 by decreasing the temperature in a 10° interval (Best 2008) [Eq. (6)]:

$$k_1/k_2 = \exp[(E_a/R) \times (1/T_2 - 1/T_1)] \quad (6)$$

The activation energy E_a for producing OH radicals is about 20 kcal/mol (Nakai and Yoneda 2000), which corresponds to 83,680 J/mol. In agreement with the Q_{10} rule proposed by van't Hoff (1884), according to Eq. (6) the rate of chemical reactions is threefold to fourfold slower at 267 K than at 277 K. This means that there is a decrease in chemical reactions by a factor of 3.9 in the considered temperature interval of 10 K. Accordingly, it is concluded that the production of OH radicals through dissociation decreases with a decrease in the room temperature from 298 K (25 °C) to 267 K (−6 °C) by a factor k_1/k_2 of about 50. In other words, the rate constant at 298 K is about 50 times greater than that at 267 K, which may lead to an increase in bond cleavages and rearrangements caused by faster movements of molecules. In everyday life, the reduced rate of biochemical degradation can be observed by preservation of food in refrigerators. Best (2008, p. 493) has underlined that "sufficiently low temperature can virtually stop chemical changes for centuries". Note that the radiation-induced DNA damage of frozen objects can be assessed using the Stokes–Einstein relation (see below in more detail), which allows the calculation of the diffusion coefficient of the hydroxyl radical at 273 K to determine its mean square displacement.

Monte Carlo toolkit

Interaction processes between elementary particles and the atoms of a cell are of stochastic nature and can be studied only by MC algorithms. Here, the radiation effects of single electrons within water-filled ellipsoid phantoms of a cell (cell size $6 \times 6 \times 10$ μm^3) were simulated by the open-source toolkit Geant4-DNA (Incerti et al. 2010). Geant4 stands for "Geometry and Tracking"; the software was developed at CERN "for the simulation of the passage of particles through matter" (Agostinelli et al. 2003). Electrons with energies of 5, 10, 15, and 20 keV were generated sequentially at the cell border to simulate single cell hits, the most dominant radiation-induced damage (Wanek et al. 2013). Other important parameters such as geometry and number of primary particles are discussed in our previous work (Wanek et al. 2013). The object-oriented C++ Geant4 toolkit for MC simulations was originally developed by theoretical physicists for high energy physics with the aim of enhancing the understanding of the complex interactions between particles and matter. The Geant4-DNA project is an extension of the general Geant4 toolkit initiated by Dr Petteri Nieminen at the European Space Agency in 2001 (Nieminen and Santin 2015) with the purpose of simulating physico-chemical phenomena in biological matter. The accuracy of "Geant4-DNA physics models for the transport of electrons in liquid water" (André et al. 2014, p. 92) was compared against several other MC codes from the literature, and it was concluded that "all of them are statistically compatible with Geant4-

DNA" (André et al. 2014, p. 92). The energy range for which validity was tested was from 4 eV to 100 keV for electrons in liquid water (Munoz et al. 2012, p. 208).

In the present study, Geant4, version 10.1 (64 bits), released in December 2014 has been used. The toolkit allows the simulation of particle and molecular species in water cell phantoms, namely hydroxyl radicals ·OH, hydrogen H·, oxonium-ions H_3O^+, dihydrogen H_2, hydrogen peroxide H_2O_2, and hydrated electrons e^-_{aq} (Incerti et al. 2010). It is assumed here that excitations and ionizations of water atoms caused by secondary electrons are responsible for the creation of free radicals (Abolfath et al. 2013). Cell hits from electrons with different energies were simulated, and the produced chemical species were assumed to form distinguishable volumes, called "Volume of Risk" (VOR).

According to our previous study (Wanek et al. 2013), incident mono-energetic electrons in the energy interval of 5 to 20 keV (Fig. 2) were considered as the most important particles which may contribute to direct and indirect damage of DNA fragments. The energy range is related to the DNA damage ranges calculated in "Results" section. In addition, the maximum energy absorption in cells (20 keV) is related to the worst-case radiation risk for DNA damage for indirect effects. Consequently, cell hits with secondary electrons were produced to study the radiochemical yields in the water phantom.

Mean energy absorption in wet cells

Figure 2 depicts the mean energy absorption in cell phantoms (normal tissue, $6 \times 6 \times 10$ µm^3) as a function of the X-ray tube voltage. The diagram in Fig. 2 shows energy absorptions in cells following exposure to secondary electrons from CT imaging. Therefore, all simulations in the present study were performed using the energy range of secondary electrons between 5 and 20 keV. Note that the diagram in Fig. 2 is based on the data of our previous study on CT-induced direct radiation effects (Wanek et al. 2013).

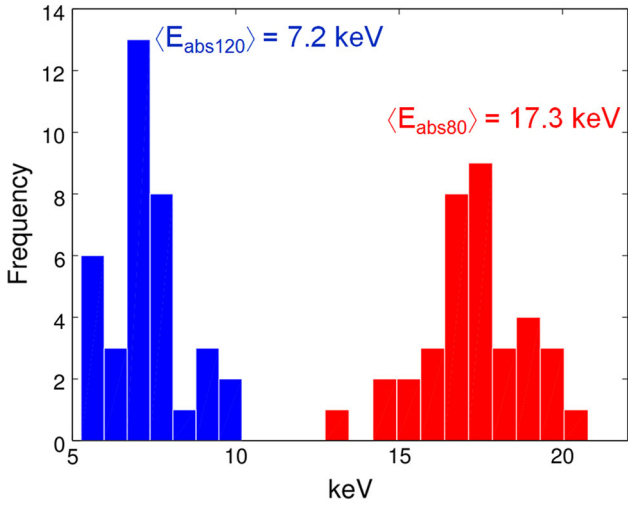

Fig. 2 Mean energy absorption in cell phantoms ($n = 85$) at different X-ray tube voltages: 80 (*red*) and 120 kVp (*blue*). Histogram shows additional unpublished data from our previous work (Wanek et al. 2013) (colour figure online)

Volume of risk in wet cell phantom

Volumes of risk were determined by Geant4-DNA simulations; then the mean cross-sectional areas for four different electron energies (5, 10, 15, and 20 keV) and chemical yields (CYs), namely $\langle A_{CY5}\rangle$, $\langle A_{CY10}\rangle$, $\langle A_{CY15}\rangle$, and $\langle A_{CY20}\rangle$, were calculated. In Fig. 3 (top), the mean cross-sectional area $\langle A_{CY}\rangle$ is shown. This area was calculated from the side view (SV) and the top view (TV) of the electron track at each energy for the construction of the 3D models. For the quantification of the mean cross-sectional areas, the Java-based image processing software ImageJ, V1.49q (Rasband 1997–2015) was deployed.

The conversion of 2D images of electron tracks and radiolytic yields to 3D models of VORs was performed with cylinder models. The cross-sectional area of the cylinder $\langle A_{CY}\rangle$ in Fig. 3 is equal to the mean cross-sectional area from CYs in cells. The length of all cylinders is given by the mean path length of secondary electrons with $\langle L_{e-5}\rangle$, $\langle L_{e-10}\rangle$, $\langle L_{e-15}\rangle$, and $\langle L_{e-20}\rangle$. The cylinder volume is $V_{cyl} = \langle \mathbf{VOR}\rangle = r^2\ \pi\ \langle L_{e-}\rangle$ with the cross-sectional

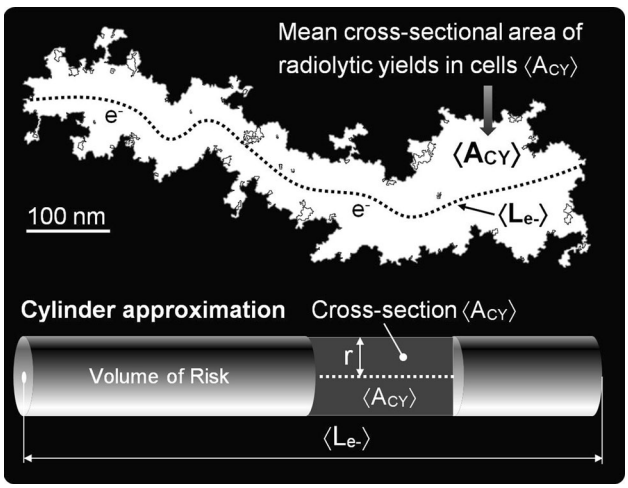

Fig. 3 *Top* result of the Geant4-DNA simulation for a certain electron energy of 5 keV (*side view*); the *dotted line* represents the track of a single electron within a cell model. Ionizations and excitations around the track structure result in the production of chemical species in a water-filled cell phantom. *Bottom* the mean cross-sectional area $\langle A_{CY}\rangle$ and the path length $\langle L_{e-}\rangle$ (821 nm) of the secondary electron are converted into a cylinder model with identical cross-sectional area and length by a cylinder approximation. The *cylinder* represents the 3D representation of all radiolytic yields per electron energy

area of the cylinder $\langle A_{CY} \rangle = 2\, r\, \langle L_{e-} \rangle$. The cylinder radius $r = \langle A_{CY} \rangle / 2\ \langle L_{e-} \rangle$ can be inserted in the equation above for V_{cyl} and one obtains Eq. (7):

$$\langle \mathbf{VOR} \rangle = \langle A_{CY} \rangle^2 \pi / 4 \langle L_{e-} \rangle \quad (7)$$

DNA fragment density from atomic force microscope images

Particular attention is paid to DNA fragments which are close enough to react with the produced radicals (Hamm et al. 1998). In order to quantify the number of randomly orientated DNA fragments within the VOR_{298}, the DNA fragment density was determined. Measurements taken by three different authors (Rivetti and Codeluppi 2001, p. 58, Fig. 2a; Sanchez-Sevilla et al. 2002, p. 153, Fig. 1b; González et al. 2012, p. 535, Fig. 2b) are shown in Table 1. It can be seen qualitatively that the DNA fragments are homogeneously distributed within an area of $2 \times 2\ \mu m^2$. In Table 1, three 2D AFM images were extrapolated to 3D space using ImageJ (Rasband 1997–2015).

The number of DNA fragments in Table 1 was automatically counted from the AFM image, and the 3D fragment density $\boldsymbol{\rho}$ was determined by the equation $\rho = (\text{number of fragm}/A_{AFM})^{3/2}$, with the image area $A_{AFM} = 4\ \mu m^2$.

Probability of DNA fragment damage at 298 K

Considering the number of base pairs per diploid cell, which is approximately 6.4×10^9 bp (EPFL 2012), the probability of DNA fragment damage $P(DI)_{298}$ (DI stands for direct and indirect effects at 298 K) in Eq. (8) induced by secondary electrons and single cell hits was estimated by the quotient $P =$ affected fragments within VOR/all fragments within the cell.

$$P(DI)_{298} = P(1) \times \langle VOR_{298} \rangle \times \langle \rho \rangle \times \langle BPS \rangle / 6.4 \times 10^9 \quad (8)$$

The factor $P(1)$ takes into account the direct radiation effects and the probability of a single cell hit in normal tissue (NT) of a wet cell (size $6 \times 6 \times 10\ \mu m^3$) with $P(1) = 0.37$, according to Poisson distribution (Wanek et al. 2013). The product $\langle VOR_{298} \rangle \times \langle \rho \rangle$ represents the number of potentially damaged DNA fragments within the VOR at 298 K. The quotient $6.4 \times 10^9 / \langle BPS \rangle$ stands for the mean number of fragments in the whole cell phantom with the mean base pair size $\langle BPS \rangle$ of 751 bp, and the fragment length would be 751×0.34 nm (length of twist) ≈ 255 nm (Table 1).

Molecular diffusion as a function of the temperature

The damage assessment of the frozen cell was carried out using the Stokes–Einstein and Einstein–Smoluchowski relations, and based on the simulation outcome of wet cell phantoms. Note that the Geant4-DNA tool was originally validated to simulate physico-chemical phenomena in biological matter, and therefore, the interacting medium was liquid and not frozen water. Therefore, the damage assessment described in this section is based on mathematical relations. According to the Stokes–Einstein equation, the diffusion coefficient D_o of chemical species is expected to decrease with decreasing temperature [Eq. (9)] (Kuhn et al. 2009).

$$D_0 = k_B T / 6\pi\eta R_H \quad (9)$$

where k_B is the Boltzmann's constant of 1.38×10^{-23} J/K, T is the absolute temperature in Kelvin, and η is the dynamic viscosity of water, which is $\eta_{298} = 0.00089$ kg/ms at 298 K and $\eta_{273} = 0.00178$ kg/ms at 273 K (Crittenden et al. 2012). According to the experimental work of Holz et al., the hydrodynamic radius R_H decreases slightly (by about 4 %) when the temperature of water decreases from 298 to 273 K (Holz et al. 2000). For the present calculations, $R_H = 0.2$ nm at 298 K from (Kuhn et al. 2009) and $R_H = 0.192$ nm at 273 K from (Holz et al. 2000) was used.

Table 1 Calculated 3D fragment density from atomic force microscopy (AFM) images

Reference	Number of fragments/4 μm^2 image	Number of fragments/μm^2 image	(Number of fragments)$^{1/2}$ = cube edge length	(Cube edge length)^3 = fragment density ρ (fragm/μm^3)	Base Pair Size (BPS) (bp)
1	114	28.5	5.3	152	1054
2	117	29.3	5.4	158	648
3	114	28.5	5.3	152	550
⟨Mean⟩	115	28.8	5.37	154	751

All DNA fragments are measured in liquids by AFM; *1* Rivetti and Codeluppi (2001), *2* Sanchez-Sevilla et al. (2002), *3* González et al. (2012)
BPS base pair size is the length of one DNA fragment measured in base pairs (bp)

Mean square displacement of chemical species

The impact of the temperature on the mobility and formation of chemical species in water is a main issue in this work. Any chemical species undergoes a random variation (Brownian movement) in liquids; however, the lifetime of radicals is generally short and is in the range of microseconds (Karamitros et al. 2011). In the present study, the movement of six different chemical species around the secondary electron is estimated for the time range between $t_0 = 1$ ps and $t_1 = 1 \times 10^5$ ps ($\Delta t \approx 1 \times 10^{-7}$ s) (Karamitros et al. 2011).

This is exactly the time range used in the Geant4-DNA simulation for radicals in the wet cell. The distance covered by radicals between t_0 and t_1 is called the "mean square displacement" (MSD). According to the Einstein–Smoluchowski relation, the MSD can be determined by Eq. (10) (Karamitros et al. 2011)

$$\langle R \rangle = \sqrt{6 \Delta t D_0} \tag{10}$$

The temperature dependence of D_0 results in different MSDs such as $\langle R_{298} \rangle$ and $\langle R_{273} \rangle$ and the corresponding volumes VOR_{298} and VOR_{273} for the temperatures 298 and 273 K (Fig. 4).

Solving Eq. (10) by substitution with Eq. (9) gives the MSD ratio at 273 and 298 K.

$$\frac{\langle R_{273} \rangle^2}{\langle R_{298} \rangle^2} = \frac{T_{273} \eta_{298} R_{\mathrm{H298}}}{T_{298} \eta_{273} R_{\mathrm{H273}}} \tag{11}$$

As shown in Eq. (11), the change of the MSD depends only on the temperature T, viscosity η , and hydrodynamic radius R_{H}.

Temperature reduction in cells results in volume changes of radiolytically formed chemical species due to the decreased displacements of molecules and the decreased reaction rates. The VOR in Fig. 4 is defined with the formulas $\langle \mathrm{VOR}_{273} \rangle = \langle R_{273} \rangle^2 \ \pi \ \langle L_{e-} \rangle$ at 273 K and $\langle \mathrm{VOR}_{298} \rangle = \langle R_{298} \rangle^2 \ \pi \ \langle L_{e-} \rangle$ at 298 K. Assuming that the mean length of the electron track $\langle L_{e-} \rangle$ is approximately identically for both temperatures, the ratio can be written as:

$$\frac{\langle \mathrm{VOR}_{273} \rangle}{\langle \mathrm{VOR}_{298} \rangle} = \left(\frac{\langle R_{273} \rangle}{\langle R_{298} \rangle} \right)^2 \tag{12}$$

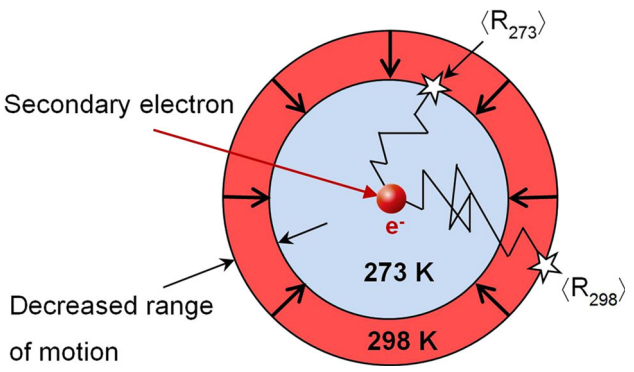

Fig. 4 Cross section of the cylinder approximation demonstrating the different VORs due to the temperature dependence of the diffusion coefficient. Note the different ranges of motion and the irregular fluctuations of the chemical species when the temperature is changed from 298 to 273 K

Probability of DNA fragment damage at 273 K

To get the probability of radiation-induced fragmented DNA damage in frozen cells [Eq. (13)], Eq. (8) was extended by the relation of Eq. (12):

$$P(\mathrm{DI})_{273} = P(1) \times \langle \mathrm{VOR}_{298} \rangle \times [\langle R_{273} \rangle / \langle R_{298} \rangle]^2 \times \langle \rho \rangle \times \langle \mathrm{BPS} \rangle / 6.4 \times 10^9 \tag{13}$$

Equations (8) and (13) represent the probability of damaging DNA fragments at 298 and 273 K for any electron energy. Consequently, the overall calculations include eight equations corresponding to four different kinetic energies of secondary electrons, namely 5, 10, 15, and 20 keV, and two different temperatures.

Results

Indirect radiation effects in wet cells

According to our previous work (Wanek et al. 2013), cells in normal tissue (NT) are mostly affected by secondary electrons and single hits. As demonstrated in Fig. 5, cell hits at varying electron energies result in different volumes of chemical yields (CYs).

DNA fragment damage (direct and indirect) in wet cells at 298 K

Table 2 shows the relationship between incident electron energy and the probability P(DI) (direct and indirect effects, DI) of DNA fragment damage. The probability was calculated by Eq. (8) for different energies of simulated electron hits (Fig. 5).

DNA fragment damage in frozen cells at 273 K

The results shown in Table 3 again demonstrate the relationship between different incident electron energies, the changes in VOR at lower temperature, and the probabilities ***P*(DI)** of DNA fragment damage. The probabilities were calculated using Eq. (13) and based on the data simulated at 298 K.

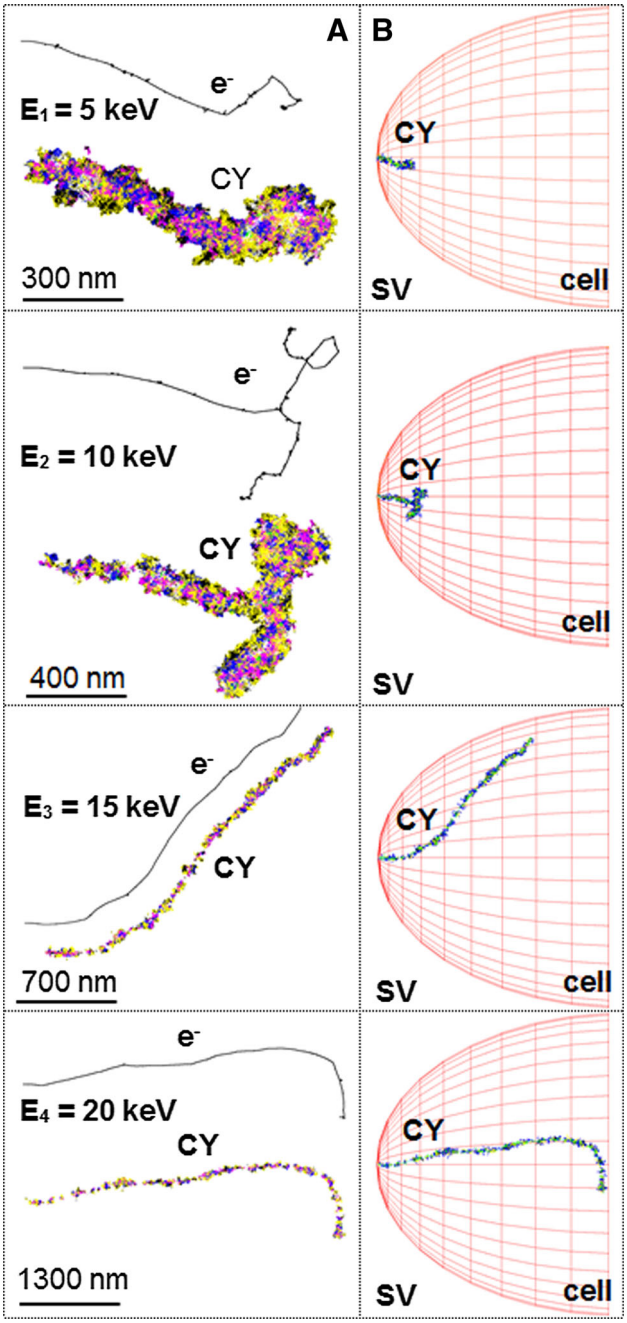

Fig. 5 *A-Top* secondary electrons e^- at different energies $E_{1\ldots4}$. *A-Bottom* chemical yields (CY) in water phantoms H· (*white*), OH· (*magenta*), H_2O_2 (*green*), H_3O (*yellow*), H_2 (*white*), and e_{aq} (*blue*) inside a phantom cell. The *coloured tracks* show the accumulated CY in the time range between 1 ps and 100 ns according to Geant4-DNA (G4Scheduler). *B* a secondary electron hits half of an elliptical cell phantom with a full size of $6 \times 6 \times 10$ μm^3. All images in this figure were taken in side view (SV) (colour figure online)

The impact of temperature and tube voltage on DNA fragment damage is shown in Fig. 6.

For comparison, Fig. 7 shows the linear relation between the DNA fragment size and the probability of damaging dry DNA fragments.

Comparative assessment of radiation damage in different physical states

Figure 8 summarizes the overall results of the worst predictor (highest p value) obtained in the present study based on simulations and calculations according to Fig. 6 for wet and frozen objects, and according to Fig. 7 for dry objects. Figure 8 also includes the highest additional cancer risk of adult humans from exposure to X-rays obtained using the X-ray cancer risk calculator (Hanley 2013). This risk was based on a 20-year-old female following CT exposure of the abdomen (Hanley 2013). Note that the risk calculator may be inaccurate for paediatrics (Hanley 2013).

Discussion

The results support both hypothesis (1) which predicts that the temperature affects the molecular diffusion of reactive species, and hypothesis (2) which predicts that the indirect radiation effects increase the probability of aDNA damage in comparison with direct effects.

Dealing with aDNA means that available computer models are limited due to the lack of structural studies on ancient cells at nanoscale. Consequently, simulations were focused in the present study on the produced chemical species in a water cell phantom following X-ray exposure. Modelling millions of DNA fragments distributed over a wide range in the ancient cell phantom is currently unrealizable. Therefore, the Geant4-DNA simulation was based on the generation of electron tracks and diffusion-controlled chemical reactions inside of phantom cells in the chemical stage at 298 K. The radiochemical yields, represented by the VORs, were simulated at 298 K and then extrapolated to 273 K using the Einstein–Smoluchowski relation. The DNA fragment concentration (fragments/μm^3) in water was determined using AFM images, and the damaged fragments were calculated by the product of the VOR and the fragment concentration. For the model calculations, the worst-case scenario was considered. It was assumed that the VORs are subsets of the volume formed by DNA fragments.

Temperature dependences in the frozen environment were described by the Einstein–Smoluchowski relation [Eq. (13)], and the VOR decreased by a factor of 0.46 [Eq. (12)] at 273 K compared to that at 298 K. Comparing Table 2 with Table 3, it was found that the VOR is approximately halved when the temperature decreases from 298 to 273 K.

The chemical species generated by the indirect action of ionizing radiation in the water cell phantom are considered to be surrounded by an envelope containing the tracks, spurs, and blobs of secondary electrons. Based on the

Table 2 Simulated probability P(DI) of DNA fragment damage (direct and indirect) in wet cells; E_{e-} electron energy; $\langle A_{CY} \rangle$ (mean cross-sectional area) and $\langle L_{e-} \rangle$ (mean electron path length): measured and calculated from the side and top view of the simulation; dE (energy loss) and ions per length—produced by simulations; volume of risk at 298 K $\langle VOR_{298} \rangle$ calculated according to Eq. (7) and normalized to 100 %

E_{e-} (keV)	$\langle A_{CY} \rangle$ (μm^2)	$\langle L_{e-} \rangle$ (μm)	dE (keV/μm)	Ions per length (ions/μm)	$\langle VOR_{298} \rangle$ (μm^3) × 10^{-2}	Damaged fragments in $\langle VOR_{298} \rangle$	P(DI) × 10^{-7}
5	0.108	0.87	5.75	333	1.05	1.6	0.7
10	0.211	2.06	4.87	195	1.7	2.6	1.1
15	0.441	3.78	3.97	148	4.04	6.21	2.7
20	0.584	5.53	3.62	106	4.84	7.46	3.2

Damaged fragments: number of potentially damaged DNA fragments with [$\langle VOR_{298} \rangle \times \langle \rho \rangle$], see Eq. (8); note that $\langle A_{CY} \rangle$ depends on the temperature of cells and the energy of the electron, while $\langle L_{e-} \rangle$ depends only on the energy of the electron

Table 3 Calculated probabilities P(DI) (*DI:* direct and indirect effects) of DNA fragment damage in frozen cells as a function of incident electron energy E_{e-}; *VOR* volume of risk

E_{e-} (keV)	VOR_{273} (μm^3) × 10^{-2}	Damaged fragments in VOR_{273}	P(DI) × 10^{-7}
5	0.5	0.8	0.3
10	0.81	1.3	0.5
15	1.93	3.0	1.3
20	2.31	3.6	1.5

CT-induced probability of fragment damage to wet and frozen cells at different tube voltages

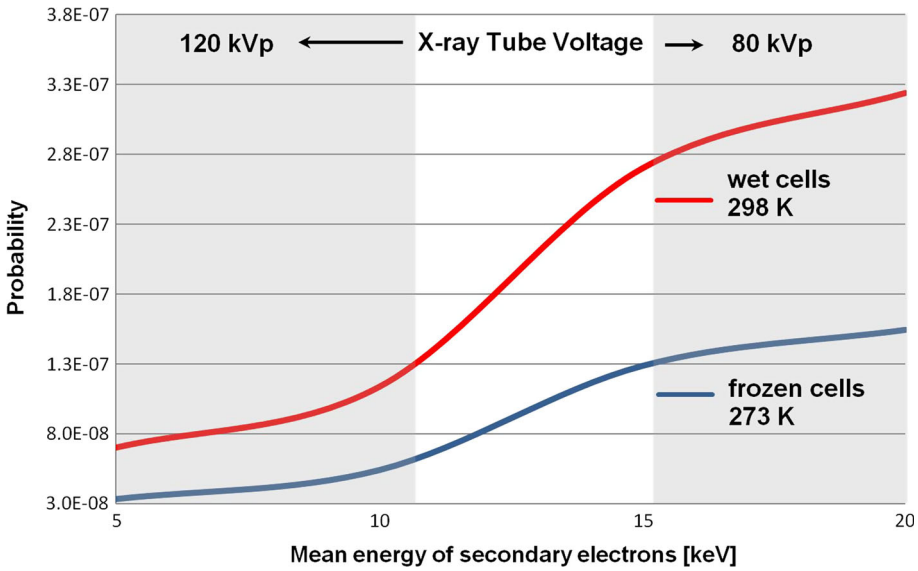

Fig. 6 Probability of CT-induced DNA fragment damage for 298 K (wet cells, *red line*) and 273 K (frozen cells, *blue line*). *Grey shaded* areas indicate the ranges where the mean energy absorption in cells reaches its maximum (according to Fig. 2) (colour figure online)

calculated cross-sectional views, different VORs were constructed. It was shown that the produced radicals within these volumes are more effective in DNA fragment damage than single direct hits in Fig. 8. This fact may explain the low probability of radiation-induced damage to dry objects exposed mainly to single hits (see Figs. 7, 8). Additional evidence for the low radiation sensitivity of dry objects is also provided by our previous work (Wanek et al. 2013). The small probability differences shown in Fig. 7 between 80 and 120 kVp are caused by the fact that at 120 kVp Compton scattering is the dominant process, while at 80 kVp photo-absorption is the dominant process (Wanek et al. 2013). Figure 6 also displays the increase in radiation damage with the decrease in the X-ray tube voltage by photo-absorption in the phantom cell. Statistically, the direct effects in dry objects are only significant for high-quality DNA samples when target volumes of DNA fragments become larger (Fig. 7).

Although Geant4-DNA simulations seem to describe particle interactions on phantom cells in a reasonable way,

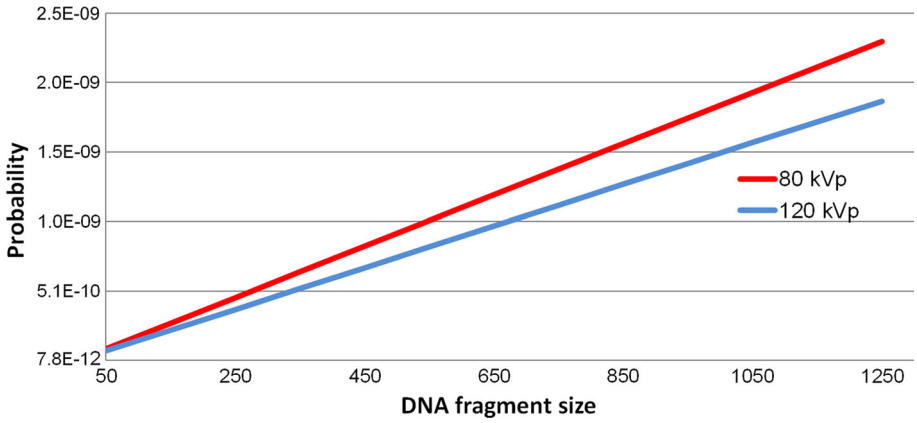

Fig. 7 Probability of damage to dry DNA fragments for two different X-ray tube voltages. The probability is calculated according to Eq. (1). The data are based on our previous work (Wanek et al. 2013)

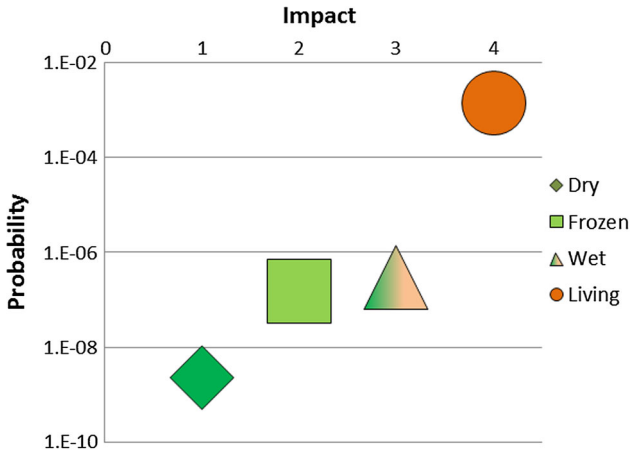

Fig. 8 Comparison of probability of damage to fragmented DNA in dry (*rhombus*), frozen, (*square*), and wet cells (*triangle*) following CT exposure and additional cancer risk (*circle*) for a 20-year-old female following CT exposure of the abdomen (Hanley 2013). Impact levels: *1* insignificant, *2* very low, *3* low, *4* Medium

the results should be validated with experimental molecular techniques. Unfortunately, experimental procedures that fulfil the requirements regarding accuracy, reliability, and reproducibility are, to the best of our knowledge, not yet available.

During the course of this work, a lack of research papers relating diffusion and DNA fragmentation in ancient cells at different physical states was noted. More research may therefore lead to a better understanding of DNA fragmentation in ancient cells and to enhanced models to be used in future simulations.

The overall findings obtained in the present work are encouraging, suggesting that desiccated mummies are not subject to a significant radiation damage following CT imaging. In the case of wet and frozen objects, forensic scientists and palaeopathologists may define the workflow in future X-ray imaging studies and molecular analyses, to minimize the radiation damage to valuable ancient remains. It was also demonstrated in the present study that the radiation damage to ancient objects is always smaller than the damage to living objects, due to DNA fragmentation and the lack of metabolism in ancient objects. The high number of DNA fragments (n) in ancient cells leads to a dramatic decrease in the hit probability of secondary electrons on nucleotides by $1/n$ [Eq. (1)]. Therefore, the impact of direct and indirect action of ionizing radiation on subunits of aDNA is smaller than the impact of low-dose ionizing radiation on normal DNA of living objects (Fig. 8), as predicted by target theory.

Conclusions

Our expectation that the temperature in liquid and frozen cells affects the radiation damage to aDNA seems correct. Stokes–Einstein–Smoluchowski calculations support this notion that the cell temperature affects the probability of radiation-induced aDNA damage, which results in a decreased indirect radiation effect in frozen cells. However, the radiation-induced aDNA damage to wet objects increases by about two orders of magnitude with $P = 10^{-6}$–10^{-7} because of the higher radical yields produced in cells at ambient temperature. Direct radiation effects on dry objects (Wanek et al. 2013) were non-significant, with the probability of aDNA damage being $P < 10^{-8}$.

As demonstrated, the physical states of ancient objects, the aDNA quality (fragmentation), and CT tube parameters may have an impact on the radiation effect of CT imaging of ancient remains and fragmented DNA. In the present work, radiation risks to living, dry, wet, and frozen objects were classified for the first time by taking into consideration direct and indirect effects (Fig. 8).

In this investigation, MC simulations, Stokes–Einstein–Smoluchowski relations, and AFM measurements were combined to quantify the aDNA damage following

CT imaging of ancient remains in dry, wet, and frozen states. Based on the data given by the Geant4-DNA simulations of wet objects at 298 K, the decrease in molecular diffusion of reactive species at 273 K was calculated. The overall radiation-induced damage on fragmented DNA in different physical states has never been addressed before.

For any genetic analysis, it is vital that the DNA quality is not affected by the applied ionizing radiation. However, CT exposure may further degrade aDNA by fragmentation. To avoid loss of genetic information, assessment of radiation damage in different physical states plays an increasing role in the case of X-ray imaging. However, several research groups demonstrated that PCR methods are not able to deliver reliable results. To overcome this gap, MC simulations of electron tracks in water phantoms were performed to assess important radiolytic effects.

Mummy researchers may ignore the radiation-induced aDNA damage to dry remains following CT imaging. The relevance of DNA fragment damage in wet objects (≈ 8 fragments per cell hit) and frozen objects (≈ 4 fragments per cell hit) must be seen in relation to the methods of molecular analysis used. In case of uncertainty, the molecular analysis should be done before the X-ray exposure is initiated.

Simulations and calculations in this study were based on worst-case scenarios, assuming that DNA fragments are homogeneous distributed within the whole cell. Additional AFM investigations on aDNA structure would be a good approach to overcome the assumption of DNA fragment distribution in future work.

Acknowledgments The authors would like to acknowledge the Mäxi-Stiftung in Zurich for generous support.

References

Abolfath RM, Calson DJ, Chen ZJ, Nath R (2013) A molecular dynamics simulation of DNA damage induction by ionizing radiation. Phys Med Biol 58(20):7143–7157

Agostinelli S, Allison J, Amako K, Apostolakis J, Araujo H, Arce P et al (2003) Geant4—a simulation toolkit. Nucl Instrum Methods A 506:250–303

Alpen EL (1998) Radiation biophysics, 2nd edn. Academic Press, San Diego

André T, Morini F, Karamitros M, Delorme R, Le Loirec C, Campos L, Champion C, Groetz JE, Fromm M, Bordage MC, Perrot Y, Barberet PH, Bernal MA, Brown JMC, Deleuze MS, Francis Z, Ivanchenko V, Mascialino B, Zacharatou C, Bardiès M, Incerti S (2014) Comparison of Geant4-DNA simulation of S-values with other Monte Carlo codes. Nucl Instrum Methods Phys B 319:87–94

Bernal MA, deAlmeida CE, Incerti S, Champion C, Ivanchenko V, Francis Z (2015) The influence of DNA configuration on the Direct strand break yield. Comput Math Methods Med 2015:417501

Best BP (2008) Scientific justification of cryonics practice. Rejuvenation Res 11:493–503

Brothwell DR (1996) European bog bodies: current state of research and preservation. In: Spindler K et al (eds) Human mummies: a global survey of their status and techniques of conservation. Springer, Vienna, pp 161–172

Brown TL, LeMay HE (1997) Chemistry: the central science, 7th edn. Prentice Hall, Upper Saddle River, pp 511–512

Crittenden JC, Trussell RR, Hand DW, Howe KJ, Tchobanoglous G (2012) MWH's water treatment: principles and design, 3rd edn. Wiley, Hoboken

Draganic IG, Draganic ZD, Adloff JP (1993) Radiation and radioactivity on the earth and beyond. CRC Press, Boca Raton

EPFL (2012) Mathematical modelling of DNA. http://lcvmwww.epfl.ch/dna_teaching/exercises/sol1.pdf. Accessed 4 Nov 2014

Foote CS, Valentine JS, Greemberg A, Liebman JF (1995) Active oxygen in chemistry. Structure energetics and reactivity in chemistry, vol 2. Chapman & Hall, New York

Geant4 (2015) http://geant4.cern.ch/. Accessed 16 Feb 2015

González LN, Arruda-Neto JDT, Cotta MA, Carrer H, Garcia F, Silva RAS, Moreau ALD, Righi H, Genofre GC (2012) DNA fragmentation by gamma radiation and electron beams using atomic force microscopy. J Biol Phys 38:531–542

Grieshaber BM, Osborne DL, Doubleday AF, Kaestle FA (2008) A pilot study into the effects of X-ray and computed tomography exposure on the amplification of DNA from bone. J Archaeol Sci 35(3):681–687

Gunderson LL, Tepper JE (2012) Clinical radiation oncology. Elsevier Saunders, Philadelphia

Haack K, Hummel S, Hummel B (2000) Ancient DNA fragments longer than 300 bp. Anthropol Anz 58:51–56

Hamm RN, Turner JE, Stabin MG (1998) Monte Carlo simulation of diffusion and reaction in water radiolysis—a study of reactant 'jump through' and jump distances. Radiat Environ Biophys 36(4):229–234

Hanley M (2013) X-ray risk. http://www.xrayrisk.com/calculator/calculator.php. Accessed 1 Aug 2013

Holz M, Heil SR, Sacco A (2000) Temperature-dependent self-diffusion coefficients of water and six selected molecular liquids for calibration in accurate ^{1}H NMR PFG measurements. Phys Chem Chem Phys 2:4740–4742

Hutchinson F (1960) Radiation inactivation of molecules in cells. Am Nat 94(874):59–70

Incerti S (2014) Geant4, low energy, electromagnetic physics. https://indico.esa.int/indico/event/89/session/4/contribution/8/material/slides/0.pdf. Accessed 11 Dec 2015

Incerti S, Ivanchenko A, Karamitros M, Mantero A, Moretto P, Tran HN, Mascialino B, Champion C, Ivanchenko VN, Bernal MA, Francis Z, Villagrasa C, Baldacchino G, Guèye P, Capra R, Nieminen P, Zacharatou C (2010) Comparison of Geant4 very low energy cross section models with experimental data in water. Med Phys 37:4692–4708

Kahan TF, Zhao R, Donaldson DJ (2010) Reactivity of hydroxyl radicals at the air–ice interface. Atmos Chem Phys 10:843–854

Karamitros M, Mantero A, Incerti S, Friedland W, Baldacchino G (2011) Modeling radiation chemistry in the Geant4 toolkit. Prog Nucl Sci Technol 2:503–508

Koenig W (1896) 14 Photographien von Roentgen-Strahlen aufgenommen im Physikalischen Verein zu Frankfurt a. M. Leipzig, Johann Ambrosius Barth

Kudryashov YB (2008) Radiation biophysics (ionizing radiation). Nova Science, New York

Kuhn H, Försterling HD, Waldeck DH (2009) Principles of physical chemistry. Wiley, Hoboken

Lea DE (1955) Actions of radiations on living cells, 2nd edn. Cambridge University Press, Cambridge

Michalik V, Spothelm-Maurizot M, Charlier M (1995) Calculated radiosensitivities of different forms of DNA in solution. Nucl Instrum Methods Phys Res B 105:328–331

Miller JH, Wilson WE, Ritchie RH (1994) Direct ionization of DNA in solution. In: Varma MN, Chatterjee A (eds) Computational approaches in molecular radiation biology: Monte Carlo methods. Plenum Press, New York, pp 65–74

Mozumder A, Hatano Y (2004) Charged particle and photon interactions with matter: chemical, physicochemical, and biological consequences with applications. Marcel Dekker, New York

Mozumder A, Magee JL (1966) Model of tracks of ionizing radiations for radical reaction mechanisms. Radiat Res 28:203–214

Munoz A, Fuss MC, Cortes-Giraldo MA, Incerti S, Ivanchenko V, Ivanchenko A, Quesada JM, Salvat F, Champion C, Garcia Gomez-Tejedor G (2012) Monte Carlo methods to model radiation interactions and induced damage. Radiation damage in biomolecular systems, biological and medical physics, biomedical engineering, Part 2. Springer, Dordrecht, pp 203–225

Nakai S, Yoneda F (2000) A theoretical investigation of (−)-deprenyl (selegiline) as a radical scavenger. Theor Chem Acc 104(5): 398–406

Nieminen P, Santin G (2015) Using the Geant4 simulation software for space research. ESA. https://sis-forum.web.cern.ch/sis-forum/public-v1/3programme/projects/Flyers/Leaflet25.pdf. Accessed 16 Feb 2015

Nikjoo H, Martin RF, Charlton DE, Terrissol M, Kandaiya S, Lobachevsky P (1996) Modelling of Auger-induced DNA damage by incorporated I-125. Acta Oncol 35:849–856

Oehrstroem L, Bitzer A, Walther M, Rühli F (2010) Terahertz imaging of ancient mummies and bone. Am J Phys Anthropol 142(3):497–500

Pääbo S (1989) Ancient DNA: extraction, characterization, molecular cloning, and enzymatic amplification. Proc Natl Acad Sci USA 86:1939–1943

Paredes UM, Prys-Jones R, Adams M, Groonbridge J, Kundu S, Agapow PM, Abel RL (2012) Micro-CT X-rays do not fragment DNA in preserved bird skins. J Zoo Syst Evol Res 50:247–250

Rae A (1996) Dry human and animal remains—their treatment at the British Museum. In: Spindler K, Wilfing H, Rastbichler-Zissernig E, Zur Nedden D, Nothdurfter H (eds) Human mummies: a global survey of their status and the techniques of conservation. Springer, New York, pp 3–8

Rasband WS (1997–2015) ImageJ. US National Institutes of Health, Bethesda, Maryland, USA. http://rsb.info.nih.gov/ij/. Accessed 10 March 2015

Rivetti C, Codeluppi S (2001) Accurate length determination of DNA molecules visualized by atomic force microscopy: evidence for a partial B- to A-form transition on mica. Ultramicroscopy 87:55–66

Rühli F, von Waldburg H, Nielles-Vallespin S, Böni T, Speier P (2007) Clinical magnetic resonance imaging of ancient dry mummies without rehydration. JAMA 298:2618–2620

Samadelli M, Melis M, Miccoli M, Vigl EE, Zink AR (2015) Complete mapping of the tattoos of the 5300-year-old Tyrolean Iceman. J Cult Herit. doi:10.1016/j.culher.2014.12.005

Samuel AH, Magee JL (1953) Theory of radiation chemistry. II. Track effects in radiolysis of water. J Chem Phys 21:1080–1087

Sanchez-Sevilla A, Thimonier J, Marilley M, Rocca-Serra J, Barbet J (2002) Accuracy of AFM measurements of the contour length of DNA fragments adsorbed on mica in air and in aqueous buffer. Ultramicroscopy 92:151–158

Semsarha F, Goliaei B, Raisali G, Khalafi H, Mirzakhanian L (2014) An investigation on the radiation sensitivity of DNA conformations to ^{60}Co gamma rays by using Geant4 toolkit. Nucl Instrm Methods Phys Res B 323:75–81

Shved N, Haas C, Papageorgopoulou C, Akguel G, Paulsen K, Bouwman A, Warinner C, Rühli F (2014) Post mortem DNA degradation of human tissue experimentally mummified in salt. PLoS ONE 9(10):e110753

Spindler K (2000) Der Mann im Eis. Neue sensationelle Erkenntnisse über die Mumie in den Ötztaler Alpen. Goldman, Munich

Than K (2011) "Wet mummy" found during roadbuilding. National Geographic. http://news.nationalgeographic.com/news/2011/03/pictures/110310-wet-mummy-china-ming-science-mummies-tomb-chinese-road/. Accessed 10 June 2015

Wanek J, Speller R, Rühli F (2013) Direct action of radiation on mummified cells: modeling of computed tomography by Monte Carlo algorithms. Radiat Environ Biophys 52:397–410

Willerslev E, Hansen AJ, Poinar HN (2004) Isolation of nucleic acids and cultures from fossil ice and Permafrost. Trends Ecol Evol 19(3):141–147

Yamaguchi H, Uchihori Y, Yasuda N, Takada M, Kitamura H (2005) Estimation of yields of OH radicals in water irradiated by ionizing radiation. J Radiat Res 46(3):333–341

Ziegler KL, Conlogue G, Beckett R, Blyth T, Aronsen PG, Fehren-Schmitz L (2013) An investigation into the effects of X-ray on the recovery of DNA from skeletal remains. The 82nd annual meeting of the american association of physical anthropologists. http://meeting.physanth.org/program/2013/session29/ziegler-2013-aninvestigation-into-the-effects-of-x-ray-on-the-recovery-of-dna-from-skeletalremains.html. Accessed 20 July 2015